HiSST: 3rd International Conference on
High-Speed Vehicle Science Technology
14 -19 April 2024, Busan, Korea

Hypersonic Flow over the Double Wedge in Low and High Enthalpy Free Stream Conditions

Anurag A. Ray[1], Ashoke De[1,2]

Abstract

The present numerical investigation addresses the hypersonic flow over the double-wedge using various gas models exposed to low and high enthalpy free stream conditions. The solver 'hyperKineticFoam' is developed in the finite volume framework, OpenFOAM© environment, capable of simulating the high-temperature effects in hypersonic flows representing vibrational and chemical non-equilibrium. This solver utilized in the present numerical investigation to address the impact of different gas models, i.e. thermally perfect gas (TPG) and thermal non-equilibrium with frozen chemistry (TNEQ) on the double-wedge configuration by exposing it to the pure Nitrogen with two different free stream conditions. One of the free stream conditions corresponds to the low enthalpy with 2MJ/kg at the inlet, while the high enthalpy represents 8MJ/kg. The preliminary results obtained by comparing the present investigation's data against the experimental results indicate negligible effects of the different gas models on the numerical solution for the low enthalpy case. At the same time, there are minute differences concerning the high enthalpy free stream conditions.

Keywords: *hypersonic flows, non-equilibrium flows, thermally perfect gas, thermal non-equilibrium gas.*

Nomenclature

Abbreviations
SBLI – Shock-boundary layer interaction.
TPG – Thermally perfect gas.
TNEQ – Thermal non-equilibrium gas.
LS – Leading edge shock
BS – Bow shock
TS – Transmitted shock
IS – Intermediate shock
TP – Triplle point
SS – Separation shock
Subscripts
1 – fore-wedge parameter
2 – aft-wedge parameter

1. Introduction

The accurate flow prediction around hypersonic vehicles with the help of numerical methodologies is a daunting task. It involves the inherent complexity of modeling the non-linear effects of vibrational energy excitation, chemical dissociation, neutral exchange reactions, and even ionization under high-temperature effects. These effects are known to dramatically alter the flow conditions over the surface of the vehicles by separating the flow from the surface, leading to peak pressure loads and high heat transfer rates that can fluctuate, leading to fatigue loads. These adverse aerodynamic loads may lead to catastrophic failure and loss of human lives. Moreover, with the advancement in aviation technology, these hypersonic non-equilibrium flow regime is not only restricted to space missions but are also expected to be evident in hypersonic civil transportation. cFASTT-1 [1] is one of the civil hypersonic airliners designed at the Centre of Future Air-Space Transportation Technology (cFASTT), intended to fly around 10 times the speed of today's modern aircraft. However, to design these vehicles, accurate

[1] *Department of Aerospace Engineering, Indian Institute of Technology Kanpur, 208016, Kanpur, India, anuragray20@iitk.ac.in*
[2] *Department of Sustainable Engineering, Indian Institute of Technology Kanpur, 208016, Kanpur, India, ashoke@iitk.ac.in*

predictions of non-equilibrium hypersonic flows are required with numerical methods, which are strenuous to date. In the past, many research groups developed solvers; among these, some of the popular numerical codes employed to perform this task are NASA's DPLR (Data-Parallel Line Relaxation by the National Aeronautics and Space Administration) [2], LAURA (Langley Aerothermodynamic Upwind Relaxation Algorithm) [3], VULCAN (Viscous Upwind algorithm for Complex flow Analysis) [4], LeMANS (The Michigan Aerothermodynamic Navier-Stokes solver) [5] and, US3D (UnStructured 3D) [6]. They have been used widely for aerodynamic calculations.

Following their footsteps, we intend to numerically replicate the sophisticated effects of non-equilibrium hypersonic flows by solving additional transport equations simultaneously along with the conventional Navier-Stokes equation. We incorporate the vibrational energy transport equations coupled with the Navier-Stokes equations and their respective source/sink terms in the OpenFOAM© framework. We use this developed solver, "*hyperKineticFoam*" to assess its viability by simulating the pure Nitrogen flow over the double wedge exposed to low and high enthalpy free stream conditions that correspond to M7_2 and M7_8 conditions tested by Swantek and Austin [7].

After this brief introduction, the article further briefly describes the computational details that briefly cover the computational domain, boundary conditions & numerical methodology, and the models required to simulate hypersonic non-equilibrium flows, followed by the present investigation's results using TPG and TNEQ gas models and comparing them with computational and experimental results available in the open literature. Finally, we conclude this article with appropriate comments on the outcomes of this study.

2. Methods and computational details

2.1. Test model and computational domain

The experimental model and the computational domain utilized in the present investigation are adapted from Ref. [8] and are shown in Fig. 1 (a) and Fig. 1 (b) respectively. The double wedge geometry consists of two deflection surfaces. The first surface (fore-wedge) is inclined at an angle of 30^0 concerning the free stream directions, whereas the other surface is inclined further by 25^0. The fore-wedge to aft-wedge ratio (L_1/L_2) is 2. This geometry replicates exactly the model tested by Swantek and Austin [7] experimentally but in two dimensions.

2.2. Boundary conditions and free stream conditions

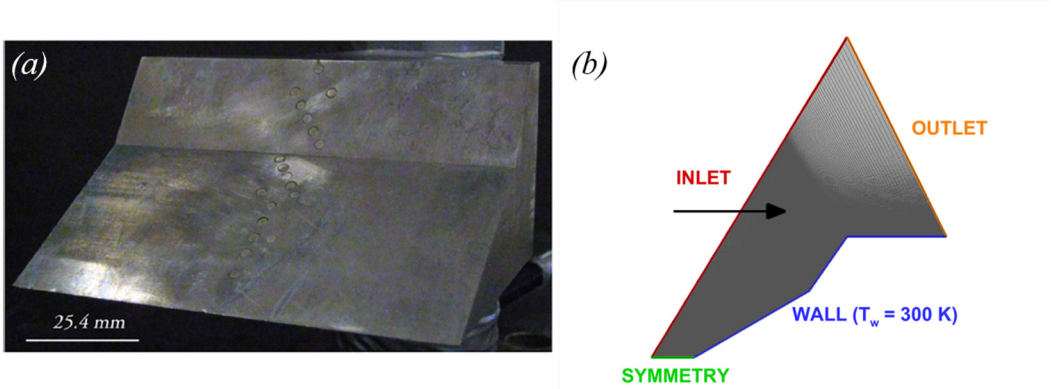

Fig 1. Experimental model (reproduced with permission) and computational domain details. (a) Experiemental model of the double wedge model. (b) Computational domain with boundary conditions.

Fig. 1 shows the computational domain employed in the present investigation. The inlet is maintained at two different free stream conditions corresponding to low and high stagnation enthalpies. These free stream conditions correspond to M7_2 and M7_8 with 2 MJ/kg and 8 MJ/kg, respectively [7]. These free stream conditions are available in Table 1. The outlet must be non-reflective; thus, we impose the wave-transmissive boundary conditions. The wall is no-slip for both the velocity and temperature,

whereas it is treated as adiabatic concerning vibrational energy transfer [9]. A symmetry boundary condition is imposed on the horizontal patch between the wedge's apex and the inlet's bottom vertex. The domain is initialized with the respective free stream conditions.

Table 1. Free stream condtions for the M7_2 and M7_8 runs [7]

Flow parameters	M7_2	M7_8
Mach number, M_∞	7.11	7.14
Stagnation enthalpy, h_0 (MJ/kg)	2.1	8.0
Static temperature, T_∞ (K)	191	710
Static pressure, p_∞ (kPa)	0.391	0.780
Velocity, U_∞ (m/s)	1972	3812
Density, ρ_∞ (kg/m^3)	0.0071	0.0038
Unit Reynolds number Re_∞, (10^6 m^{-1})	1.10	0.435
Test time, τ_t (μs)	327	242

2.3. Governing equations and thermo-physical models

We solve the standard laminar Navier-Stokes equation representing mass, momentum, and energy conservations and an additional transport equation with a source term for modeling the vibrational-translational energy exchange but with the frozen chemical reactions. The gas is assumed to behave as an ideal gas. They are listed down below for convenience.

$$\frac{\partial \rho}{\partial t} + \frac{\partial \rho u_j}{\partial x_j} = 0 \tag{1}$$

$$\frac{\partial \rho u_i}{\partial t} + \frac{\partial \rho u_i u_j}{\partial x_j} = -\frac{\partial p}{\partial x_i} + \frac{\partial \tau_{ij}}{\partial x_j} \tag{2}$$

$$\frac{\partial \rho \varepsilon}{\partial t} + \frac{\partial}{\partial x_j}\left(\rho \varepsilon + p\right) u_j = -\frac{\partial q_j}{\partial x_j} + \frac{\partial \tau_{ij} u_i}{\partial x_j} \tag{3}$$

Eq. 1 represent mass conservation equation where, ρ is the density of the fluid and u_j is the velocity component in i^{th} direction. Eq. 2 is the governing equation representing the momentum conservation where p is the pressure in the fluid element and τ_{ij} is the shear stress tensor. The fluid in this article is assumed to be obey the Newtonian law. Eq. 3 further represent the energy conservation equation with ε as the total energy of the fluid element which comprises of the internal energies corresponding to various modes e.g. translational, rotational and vibrational energy (for poly-atomic species, e.g. Nitrogen (N_2)) along with the kinetic energy of the flow. q_{ij} is the heat flux vector which uses the Fourier's law of heat conduction considering the contribution of all the energy modes in the system. They are formulated below as Eq. 4 and Eq. 5

$$\varepsilon = e + \frac{1}{2} u_j u_j \tag{4}$$

$$q_j = -k \frac{\partial T}{\partial x_j} - \frac{\partial T^{vib}}{\partial x_j} \tag{5}$$

Here, e is the internal energy of the gas which comprises of the rotational, translational and vibrational modes of energy for the polyatomic species, as mentioned above. The translational and rotational mode of energy are at complete equilibrium at sufficiently high temperatures and is represented by the trans-rotational temperature (T). The vibrational energy mode is assumed to be in equilibrium with the translational and rotational mode of energy for the 'Thermally Perfect Gas (TPG) assumptions' while they are in non-equilibrium for the Thermal Non-Equilibrium (TNEQ) gas model. The TPG gas can be modelled by assuming the sepcfic heats (c_p and c_v) as a function of temperature through Joint Army Navy Air Force (JANAF) coefficents. Therefore,

$$e(T) = h_f^o + \int_{T_{ref}}^{T} c_v(T)dT \tag{6}$$

$$h(T) = h_f^o + \int_{T_{ref}}^{T} c_p\left(T\right)dT \tag{7}$$

h_f^o is the standard enthalpy of formation for the species. On the other hand, extra transport equations are solved for each poly-atomic species in conjunction with the standard Navier-Stokes equations for determining the contribution of the vibrational energy mode towards the internal energy mode of the species. It is represented in the following manner.

$$\frac{\partial \rho e^{vib}}{\partial t} + \frac{\partial \rho e^{vib} u_j}{\partial x_j} = -\frac{\partial q_j^{vib}}{\partial x_j} + \dot{\omega}^{vib} \tag{8}$$

Here, all the symbols have the usual meaning but only the vibrational energy mode constributes to its diffusion, i.e. $q_j^{vib} = -k^{vib}\frac{\partial T_\alpha^{vib}}{\partial x_j}$. The source term of this vibrational energy transport is formulated using the Landau-Teller expression [10].

$$\dot{\omega}^{vib} = \rho\frac{e^{vib*}(T) - e^{vib}(T^{vib})}{\tau_\alpha} \tag{9}$$

with $e_\alpha^{vib*}(T)$ as the equilibrium vibrational energy evaluated at the transrotational temperature whereas, $e_\alpha^{vib}(T^{vib})$ is the vibrational energy of the di-atomic species evaluated at the vibrational temperature of the molecule. The relaxation time is calculated based on the formulation of Millikan-White expression [11] i.e.,

$$\tau_{\alpha\beta} = \frac{1}{p}\exp\left[A_{\alpha\beta}\left(T^{-\frac{1}{3}} - B_{\alpha\beta}\right) - 18.42\right] \tag{10}$$

$$A_{\alpha\beta} = 0.00116\mu_{\alpha\beta}^{\frac{1}{2}}\Theta_\alpha^{vib\frac{4}{3}} \tag{11}$$

$$B_{\alpha\beta} = 0.015\mu_{\alpha\beta}^{\frac{1}{4}}, \mu_{\alpha\beta} = \frac{\mu_\alpha\mu_\beta}{\mu_\alpha + \mu_\beta} \tag{12}$$

$$\tau_\alpha = \frac{\sum_{\beta=1}^{n} X_\beta}{\sum_{\beta=1}^{n} X_\beta \tau_{\alpha\beta}^{-1}} \tag{13}$$

Here, α and β are colliding pairs, Θ_{α}^{vib} is the characteristic vibrational temeperature of the di-atomic molecule. $\mu_{\alpha\beta}$ is the reduced effective mass of the collinding pair of species and X represents the molar fraction of the species. Ideal gas equation is used to update the pressure field. The other relevant details related to diffusion models and constants of the vibrational energy equation are availble in Ref. [9, 12].

2.4. Numerical details

The present numerical investigation employs *'hyperKienticFoam'* which uses Kurganov-Noelle-Petrova (KNP) convective flux discretization scheme, along with the TVD-based, Van Leer reconstruction scheme to facilitate the interpolation of the primitive variables on the cell interface from its either sides. This combination of the scheme provides the least dissipation and at the same time ensures sufficient stability to the code [13]. Furthermore, time integration is facilitated by the low storage, third-order accurate explicit Runge-Kutta time integration ensuring high scalability and accuracy in contrast with the standard operating splitting approach handling separate integration strategies concerning the inviscid and viscous terms' integration [14]. On the contrary, simple implicit integration is facilitated for the vibrational transport equation ensuring the stability of the integration of the transport equation with the source term. The time step is derived from the convection time scale using the Courant (CFL) number along with the viscous dissipation time scales concerning the momentum and thermal diffusion process. The least value of the time step from these stability criteria is employed in the present investigation ensuring the stable operation of the code.

3. Results and discussion

3.1. Low Enthalpy

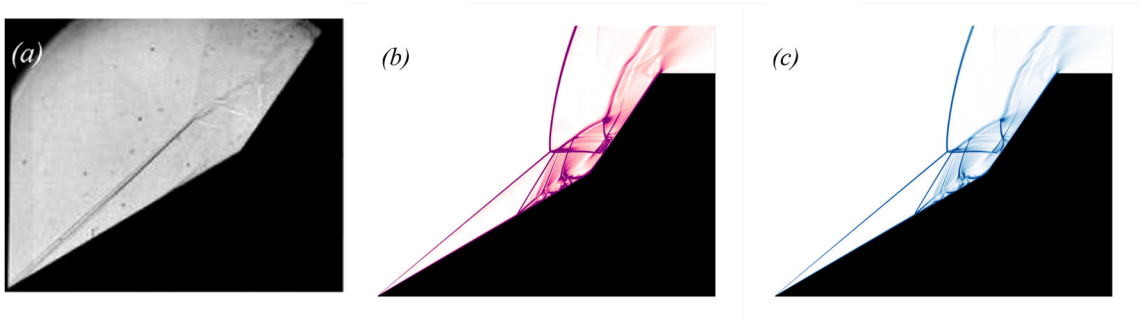

Fig 2. Experimental and numerical schlieren images at t = 150 μs at M7_2 free stream conditions (a) Experiment. (b) Thermally perfect gas. (c) Thermal non-equilibrium gas. (Experimental data reproduced with permission)

Fig. 2 depicts the numerical schlieren at 150 μs for the M7_2 free stream condition, which were experimentally examined by Swantek and Austin [7] using the TPG (magenta) and TNEQ (blue) gas models and are further compared against the experimental schlieren image. Both numerical results produce the salient flow features, such as the leading edge shock (LS) interacting with the bow shock (BS) at the triple point, to produce the Edney type-V interaction locally. A transmitted shock (TS) and a shear layer emanate from this triple point. The former impinges on the aft-wedge to create an adverse pressure gradient and promote the primary separation bubble's growth at the compression corner. Furthermore, tiny secondary separations beneath this primary separation bubble are evident in the numerical solution at this instant. These secondary separations are responsible for the unsteadiness in the flow [15].

The flow is still developing under the influence of the adverse pressure gradient by TS. The qualitative comparison is extended beyond 150 μs to examine the influence of the non-equilibrium effects on the flow field when the separation bubble enlarges significantly. Fig. 3 depicts the numerical schlieren using the TPG (magenta) and TNEQ (blue) gas models at t = 260 μs, and are compared with the experimental schlieren image. The separation bubble enlarges by the continuous influence of TS. The separation shock (SS) significantly moves upstream irrespective of the gas models and at the same time, the

impingement point over the aft-wedge surface moves downstream. The separation shock interacts with the leading edge shock forming an intermediate shock (IS) wave that further interferes with the bow shock at the triple point.

This qualitative analysis reveals no subtle differences in the flow field concerning the different models, as the bow shock's standoff distance is nearly the same at this relatively free stream condition. It is perhaps due to the low free stream enthalpy at the inlet, which is not sufficient enough to trigger the Nitrogen molecule's vibrational energy mode.

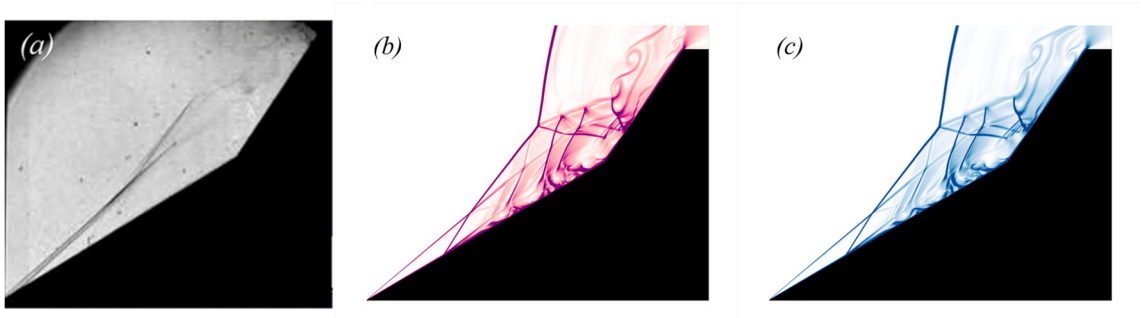

Fig 3. Experimental and numerical schlieren images at t = 260 μs at M7_2 free stream conditions (a) Experiment. (b) Thermally perfect gas. (c) Thermal non-equilibrium gas. (Experimental data reproduced with permission)

Fig. 4 (a) and Fig. 4 (b) provide the quantitative validation of the developed solver in the form of wall heat flux distribution over the surface of the double wedge compared against the experimental data both in short and wide time averaging windows, respectively. The narrow time-averaging window is considered between 150 μs and 310 μs [16] whereas the wide time-averaging window is between 0 μs and 400 μs [15]. The present investigation's wall heat flux distribution significantly overpredicts the experimental peak heat flux value irrespective of the gas models. However, the results improve substantially for the results obtained by using the wide averaging window for both models. Once again, this quantitative comparison reveals that there are no significant differences in the heat flux distribution between the models irrespective of the time-averaging windows, corroborating the above qualitative analysis.

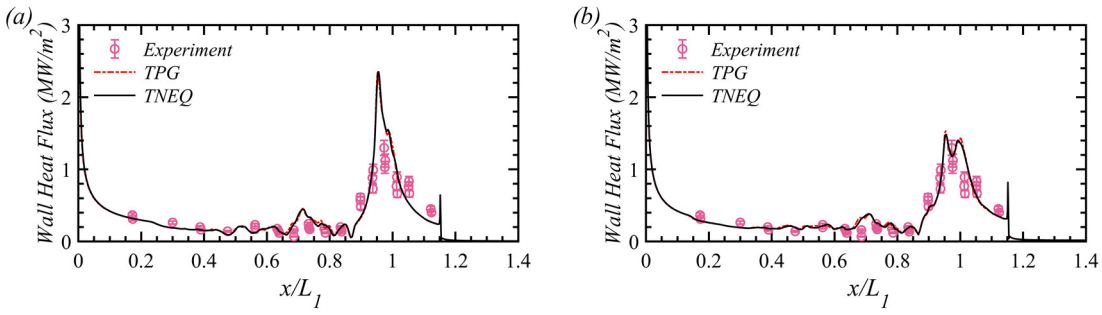

Fig 4. Mean heat flux distribution over the surface of the cylinder for M7_2 free stream conditions. (a) Narrow window. (b) Wide window. The error bars correspond to 8% uncertainty in the experiments [7].

The two-dimensional flow field is highly unsteady because of the transmitted shock impinging on the af-wedge surface and its influence propagating upstream through the subsonic portion of the boundary layer [16]. Fig. 5 is a brief elaboration of the unsteady process underlying this two-dimensional interaction mechanism. It shows the numerical schlieren images at some of the prominent time instances identified by Durna et al. [16] using the TNEQ gas model. Fig. 5 (a) to Fig. 5 (c) depicts the initial development of the flow field when the LS and BS are still establishing. The SS and and RS merge and interact indirectly with TS forming a Mach Stem (MS) and two new TPs. The TP situated away from the surface is referred to as the Upper Tripple Point (UTP) and the other near the double wedge's

surface is referred to as the Lower Tripple Point (LTP) in literature [catarina]. The additional set of shock waves emanates from these newly formed TPs one of which (originating from UTP) impinges on the shear layer and turns it away from the surface and the other shock wave now forms TS that impinges on the aft-wedge surface and thus imposes the adverse pressure gradient to the boundary layer. The flow field confined between the shear layer emanating from UTP and the double-wedge's surface, behind the Mach stem is subsonic and it gradually accelerates to the supersonic regime of the flow.

Durna et al. [16] reported that after 100 μs the primary triple point moves upstream as the BS standoff distance increases by the net increase in the deflection angle due to the thickening of the boundary layer. We see a similar behavior using the TNEQ model. Furthermore, the SS starts to propagate upstream which consequently enlarges and expands the separation bubble. The swelling of the separation region promotes the growth of the secondary separation beneath it as pointed out earlier in this article. The separation bubble rapidly expands as the separation point moves continuously upstream and thus the shock interference transits from Mach reflection to regular reflection. To summarize, the solver is capable of predicting this complex interaction of the shock waves and they are in decent agreement with the unsteady results obtained by Durna et al. [16] Furthermore, there is an insignificant impact of the gas models at this relatively low enthalpy free stream conditions.

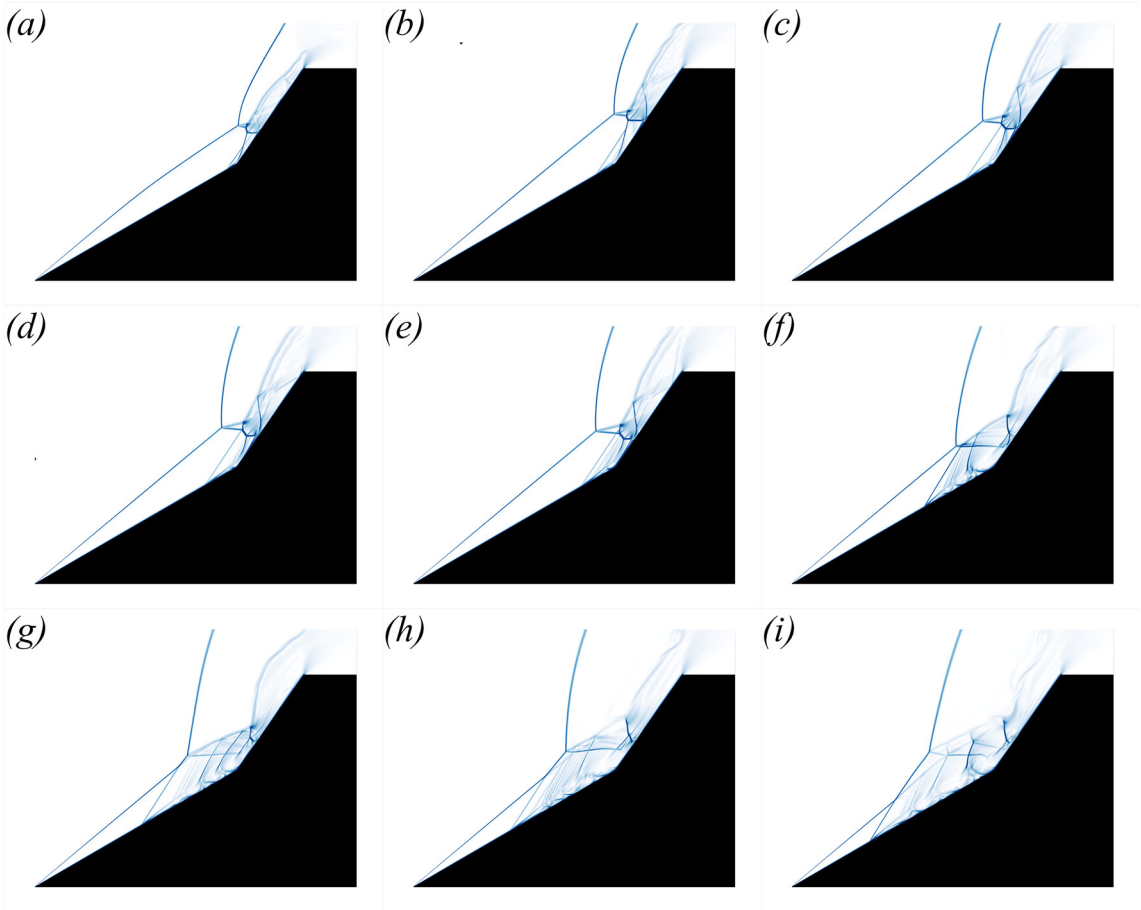

Fig 5. Numerical schlieren depicting transient flow field evolution at M7_2 free stream conditions at different instants of time. (a) 30 μs. (b) 60 μs. (c) 90 μs. (d) 100 μs. (e) 110 μs. (f) 150 μs. (g) 180 μs. (h) 210 μs. (i) 240 μs.

3.2. High Enthalpy

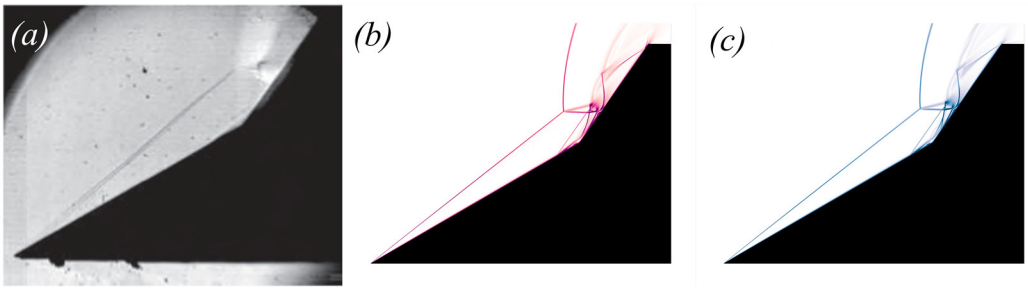

Fig 6. Experimental and numerical schlieren images at t = 60 μs at M7_8 free stream conditions (a) Experiment. (b) Thermally perfect gas. (c) Thermal non-equilibrium gas. (Experimental data reproduced with permission)

This section of the article reports the simulation of the shock interaction process using two different gas modes at relatively higher enthalpy free stream conditions. Fig. 6 compares the numerical schlieren at t = 60 μs from the present investigation using both the models with the experimental schlieren image at Swantek and Austin's M7_8 free stream conditions [7]. Once again, all the features and shock waves corresponding to the M7_2 conditions are also resolved by the solver for this case. However, the shock angles are less and the bow-shock wave lies much closer to the surface of the body in contrast to low enthalpy conditions. Furthermore, the bow shock wave's standoff distance, the oblique shock wave's angle, and the separation bubble size are slightly lower in the non-equilibrium gas model than in the TPG model. This is predominantly due to discrepancies in the shock speed in the thermal equilibrium and non-equilibrium flows [9].

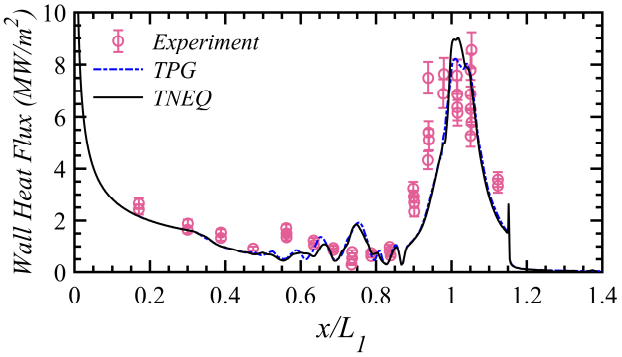

Fig 7. Mean heat flux distribution over the surface of the cylinder for M7_8 free stream conditions using TPG and TNEQ gas models. The error bars correspond to 8% uncertainty in the experiments [7].

Fig. 7 compares the mean wall heat flux for the M7_8 free stream conditions obtained using the two different gas models against the experimental data of Swantek and Austin [7]. The averaging window is fixed between 100 μs and 242 μs as suggested by Hao et al. [17]. The distribution is similar and corroborates with both numerical schlieren images as described in Fig. 6; however, there is a significant difference in the peak heat flux magnitude. It is 12.5 % higher in the case of the TNEQ model than the TPG model. The incomplete energy exchange (during the extreme ends of the averaging window) between the trans-rotational and vibrational energy modes in the case of the non-equilibrium model is responsible for the amplified peak heat flux at $x/L_1 = 1$.

Fig. 8 comprehends the unsteady interaction process with the aid of numerical schlieren images using the TNEQ gas model that lasts till the end time of the experimental duration. These figures highlight considerable differences between the flow fields corresponding to M7_2 and M7_8 free stream conditions. The shock waves do not interact indirectly and therefore the complexity of the shock structure is less severe. The LS and BS are established during the first 60 μs however, the BS standoff

distance increases gradually and consequently leads the triple point to traverse upstream. At the same time, the separation point moves closer to the leading edge significantly enlarging and expanding the separation bubble. Thus prominent secondary separations from beyond 60 μs. The continuous upstream movement of the separation point leads the SS to refract with LS. The refracted SS confluences with the BS at TP while the refracted LS interacts with TS downstream of TP. The re-attachment point of the separated shear layer starts rapidly propagating downstream increasing the size of the separation bubble significantly. The flow field appears to be highly unsteady even during the experimental end time as TS still impinges over the aft-wedge surface at this instant. Note that the interaction process here such as the expansion of the separation bubble is rapid compared to the M7_2 free stream conditions. It is thus inferred that the strength of TS shock for this free stream condition is higher promoting rapid relaxation of the flow in the form of separation bubble's expansion.

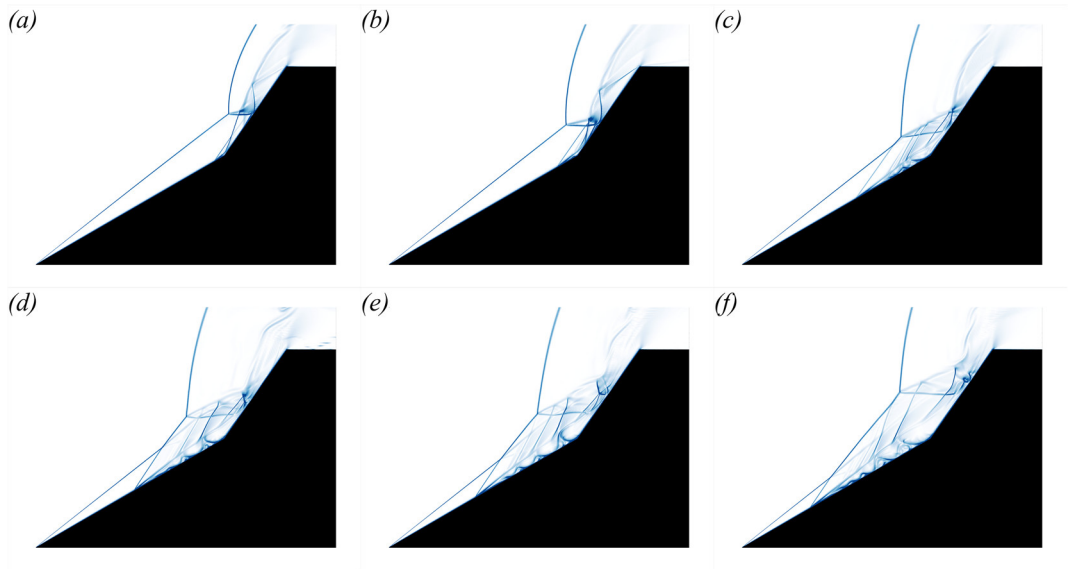

Fig 8. Numerical schlieren depicting transient flow field evolution at M7_8 free stream conditions at different instants of time. (a) 30 μs. (b) 60 μs. (c) 120 μs. (d) 150 μs. (e) 180 μs. (f) 242 μs.

4. Conclusions

The developed open-source solver '*hyperKineticFoam*' is utilized in the numerical simulation for the hypersonic flow over the double-wedge corresponding to M7_2 and M7_8 free stream conditions using pure Nitrogen as the working fluid. The results using thermally perfect gas and thermal non-equilibrium gas models are compared with the experimental results of Swantek and Austin for both conditions using qualitative and quantitative analysis. The simulation results suggest that the gas models have negligible effects on the flow features and the heat-flux distribution for the low-enthalpy conditions. They corroborate well with the experimental observations. The low enthalpy at 2MJ/kg is not sufficient enough to trigger the vibrational mode of the Nitrogen molecule. Nevertheless, we examine the unsteady process at M7_2 free stream conditions and analyze the unsteady events during the run time of experiments. The M7_2 free stream conditions reveal Edney type-V interaction with a Mach reflection and it transforms back to regular reflection during the latter course of time.

We further examine the results for the high enthalpy free stream conditions and reveal that the flow structure is slightly altered with the lower shock standoff distance and shock angles in the non-equilibrium due to differences in the shock speeds. The gas modeling impacts the wall heat flux distribution where the peak heat flux increases by 12.5 % in the case of the TNEQ gas model in contrast to the TPG gas model due to incomplete energy exchange between the energy modes of the Nitrogen molecule. The unsteady events at these free stream conditions reveal a Type-V interaction process with regular reflection from the beginning of the simulation time, unlike the low enthalpy's simulated flow field. The TS is stronger at these free stream conditions resulting in rapid expansion of the separation

bubble and thus evolves to a complex interference pattern near the end time of the experiment. The flow does not attain a steady state as transmitted shock still impinges over the surface at 242 μs.

References

1. Wuilbercq, R., Pescetelli, F., Mogavero, A., Minisci, E., Brown, R.E.: Robust multidisciplinary design and optimisation of a reusable launch vehicle. In: Proceedings of the 19th AIAA International Space Planes and Hypersonic Systems and Technologies Conference, Atlanta, GA, USA, (2014)
2. Candler, G.V.,Write, M.J., McDonald, J.D.: Data-parallel lower-upper relaxation method for reacting flows. AIAA J. 32(12) 2380–2386 (1994)
3. Cheatwood, F.M., Gnoffo, P.A.: User's Manual for the Langley Aerothermodynamic Upwind Algorithm (LAURA), Technical Report. NASA Langley Research Center, Hampton, VA, USA (1996)
4. VULCAN-CFD Official Website, http://vulcan-cfd.larc.nasa.gov/, last accessed 2016/9/4
5. Scalabrin, L.C., Boyd, I.D.: Development of an unstructured navier-stokes solver for hypersonic nonequilibrium aerothermodynamics. In: Proceedings of the 38th AIAA Thermophysics Conference, Toronto, ON, Canada (2005)
6. Nompelis, I., Drayna, T.W., Candler, G.V.: Development of a hybrid unstructured implicit solver for the simulation of reacting flows over complex geometries. In: Proceedings of the 34th AIAA Fluid Dynamics Conference and Exhibit, Portland, OR, USA (2004)
7. Swantek, A. and Austin, J.: Heat transfer on a double wedge geometry in hypervelocity air and nitrogen flows. In: 50th AIAA Aerospace Sciences Meeting including the New Horizons Forum and Aerospace Exposition, (2012)
8. Ray A., De, A.: Leading-edge bluntness effects on the hypersonic flow over the double wedge at multiple aft-wedge angles. Physics of Fluids 35, 056116 (2023)
9. Vatansever, D., Celik, B.: Unsteady shock interaction mechanisms of high enthalpy reacting flows over double wedges at Mach 7. Physics of Fluids 33, 056110 (2021)
10. Landau, L., Teller, E.: On the theory of sound dispersion. Physikalische Z. Sowjetunion 10, 34-43 (1936)
11. Millikan, R.C., White, D.R.: Systematics of vibrational relaxation. J. Chem. Phys 39, 3209-3213 (1963)
12. Kianvashrad, N., Knight, D.D.: Simulation of hypersonic shock wave laminar boundary layer interaction on hollow cylinder flare, part II. In 47th AIAA Fluid Dynamics Conference (p. 3975).
13. Greenshields, C. J., Weller, H. G., Gasparini L., and Reese, J. M.: Implementation of semi-discrete non-staggered central schemes in a collocated, polyhedral, finite volume framework, for high-speed viscous flows. J. Numer. Methods Fluids 63, 1-21 (2010)
14. Sibo, L., Paoli, R. and Mello, M.D.: Scalability of OpenFOAM density-based solver with Runge-Kutta temporal discretization scheme. Sci. Program 1-11 (2020)
15. Kumar G., De, A.: Role of corner flow separation in unsteady dynamics of hypersonic flow over a double wedge geometry. Physics of Fluids 33, 036109 (2021)
16. Durna A.S., M. El Hajj Ali Barada, and Celik B.: Shock interaction mechanisms on a double wedge at Mach 7 Physics of Fluids 28, 096101-096399 (2016)
17. Hao, J., Wen, C.Y. and Wang, J.: Numerical investigation of hypervelocity shock-wave/boundary-layer interactions over a double-wedge configuration. International Journal of Heat and Mass Transfer 138, 277-292 (2019)